Diurnal signals in satellite sea surface temperature measurements

Chelle L. Gentemann,[1] Craig J. Donlon,[2] Alice Stuart-Menteth,[3] and Frank J. Wentz[1]

Received 16 September 2002; accepted 10 December 2002; published 14 February 2003.

[1] During the daytime, solar heating may lead to the formation of a near-surface diurnal warm layer, particularly in regions with low wind speeds. This effect can be clearly seen in global, satellite-derived, maps of the difference between daytime and nighttime SSTs. Analysis of TMI and AVHRR SSTs revealed that the onset of warming begins as early as 8 AM and peaks near 3 PM., with a magnitude of 2.8 C during favorable conditions. After this peak, the signal decays gradually until 11 PM, when the skin temperature approaches the bulk temperature. An empirical model is calculated from satellite SST and wind speed data, then used to derive daily global maps of diurnal warming. When modeled warming is removed from daytime SSTs, the mean and standard deviation of day minus night SST differences are diminished. *INDEX TERMS:* 4275 Oceanography: General: Remote sensing and electromagnetic processes (0689); 4504 Oceanography: Physical: Air/sea interactions (0312); 4572 Upper ocean processes; 4231 Equatorial oceanography. **Citation:** Gentemann, C. L., C. J. Donlon, A. Stuart-Menteth, and F. J. Wentz, Diurnal signals in satellite sea surface temperature measurements, *Geophys. Res. Lett.*, *30*(3), 1140, doi:10.1029/2002GL016291, 2003.

1. Introduction

[2] During the day, in clear sky, calm conditions, thermal stratification of the top few meters of the ocean will occur [*Price et al.*, 1986]. Surface temperature deviations greater than 3°C, referenced to subsurface temperatures, are not uncommon [e.g., *Yokoyama et al.*, 1995] and may persist for hours. Since sea surface temperature (SST) retrievals by satellites are sensitive to a thin surface layer, this diurnal warming effect strongly influences these measurements. Accurate global coverage maps of SST are required for many applications including numerical weather prediction and climate research. Since large areas of the ocean are devoid of in situ instrumentation, SST must be derived from radiometers aboard orbiting spacecraft. In the future, a single optimal SST field may be provided by a fusion of these observations together with in situ measurements [e.g., *Donlon et al.*, 2002]. The different satellite and in situ data are obtained at different local times within the diurnal period, and therefore the diurnal cycle must be modeled before different data sets can be merged to derive analyzed SST products. In this paper we use satellite observations to investigate the character of global SST diurnal signals. The diurnal amplitudes are then used to construct a simple empirical model of diurnal warming for each sensor. Model skill is then examined through comparison of global patterns revealed by day minus night SST differences. Finally we present a short discussion and our conclusions.

2. Observations

[3] We use well-established analyses of satellite derived infrared SST, microwave SST, and wind speed. For infrared SST we use thirteen years (1988 through 2001) of the Oceans Pathfinder SST (PF) [*Kilpatrick et al.*, 2001] and, for microwave SST, four years (1998 through 2001) of the Tropical Rainfall Measuring Mission (TRMM) Microwave Imager (TMI) SST [*Wentz et al.*, 2000]. NOAA advanced very high resolution radiometer (AVHRR) data, which are used to produce the PF SST have an ascending equatorial local crossover time of about 1:40 PM local time that drifts to a later crossover time as the satellite ages. This limits the temporal sampling of the diurnal cycle by infrared sensors. The presence of clouds further limits infrared sensors spatial and temporal coverage, results in SST data sets that are temporally and regionally sampled at specific times of day. In contrast, the TMI equatorial orbit precesses through the diurnal cycle every 23 days, allowing complete temporal resolution of diurnal amplitudes. Furthermore, TMI data are not influenced by the presence of clouds.

[4] Our bulk SST is the Reynolds Optimum Interpolated (OI) SST [*Reynolds and Smith*, 1994], a weekly global 1° resolution SST field derived from AVHRR and in situ SST observations. Diurnal signals are minimized in the dataset through weekly averaging and by giving nighttime AVHRR retrievals a higher weight.

[5] Finally, we use near-surface daily average wind speed derived from the Defense Meteorological Satellite Program (DMSP) Special Sensor Microwave/Imager (SSM/I) [*Wentz*, 1997] and TRMM-TMI [*Wentz et al.*, 2000].

3. Analysis and Results

[6] PF and TMI SST are analyzed for diurnal warm layer effects based on the residual signal after subtracting OI SST. The diurnal amplitudes revealed are then used to construct an empirical model of diurnal warming for both TMI and PF SST. Model skill is examined through comparison of global patterns in day minus night PF SST differences.

[7] PF SSTs were collocated with daily average SSM/I wind speeds, OI SST fields, and insolation. The daily average clear sky insolation is calculated as the daily average solar energy per unit area over the top of the global atmosphere as a function of latitude and day of year following *Liou and Kuo-Nan* [1980]. Local time was approximated by the daily local equatorial crossover time found in ephemeris data. TMI retrievals provide simulta-

[1]Remote Sensing Systems, Santa Rosa, California, USA.
[2]CEC-Joint Research Centre, Space Applications Institute, Marine Environment Unit, Ispra, Italy.
[3]School of Ocean and Earth Science, Southampton Oceanography Center, Southampton, United Kingdom.

0094-8276/03/2002GL016291$05.00

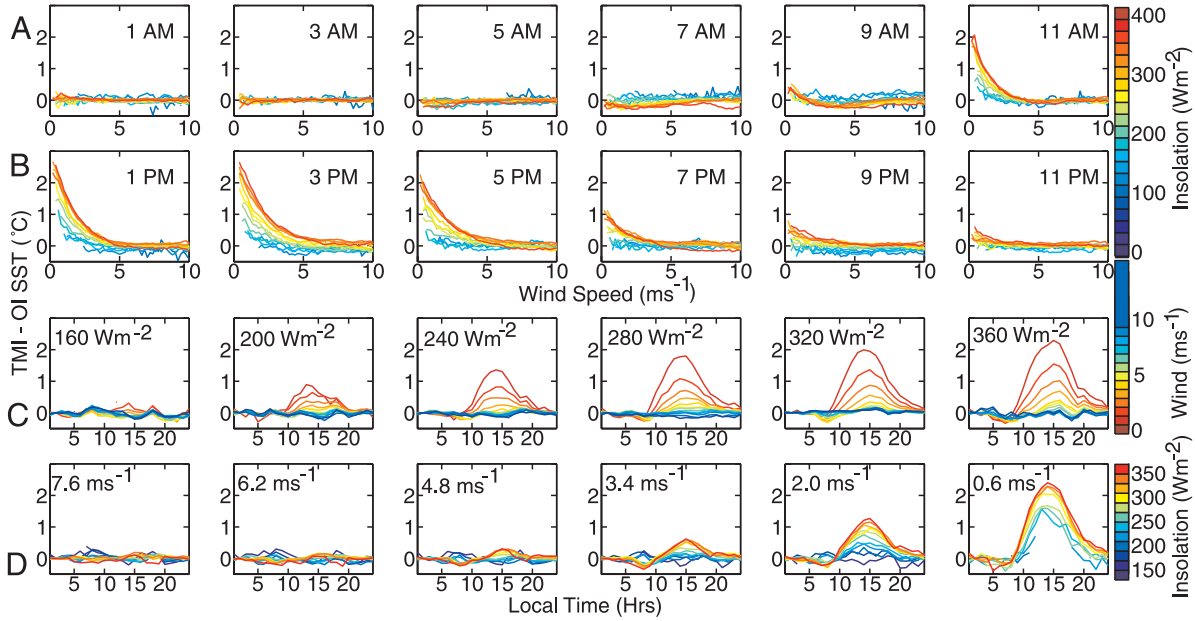

Figure 1. Diurnal warming from TMI. Rows A and B show ΔSST_{TMI} as a function of wind speed through the diurnal cycle. Daily average insolation is indicated by the color of the lines. Row C shows ΔSST_{TMI} through the diurnal cycle at several insolation values, with different wind speeds indicated by line color. Similarly, row D shows ΔSST_{TMI} through the diurnal cycle at several wind speeds, with insolation indicated by line color.

neous wind speed, SST, and time of observation. Although TMI retrieves SSTs through clouds, to simplify the analysis, only clear sky (as determined by TMI measured cloud liquid water) values were included.

[8] Collocated wind speed and insolation were used to construct the mean satellite SST minus OI SST (ΔSST) as a function of local time, wind speed, and insolation. At high wind speeds, the ocean is sufficiently well mixed that skin (PF), sub-skin (TMI), and bulk (OI) retrievals should have a constant zero bias. In reality, differences due to a combination of sensor, algorithm, and depth of measurement differences cause a small constant offset above 8.0 ms^{-1} for TMI and 11.0 ms^{-1} for PF. Below these wind speeds, the differences increase due to diurnal warming effects. To remove dataset differences and better isolate diurnal effects, the mean ΔSST at high wind speeds was calculated at each local time, and removed from the data. We next removed the nighttime cool skin to focus only on diurnal warming amplitudes, by subtracting the 2 AM ΔSST from the ΔSST at all other local times. Both TMI and PF SSTs had small biases relative to OI that were removed by this process.

[9] The influence of wind speed and top-of-atmosphere average daily insolation on diurnal warming is shown in Figure 1. At 2-hour intervals, ΔSST_{TMI} is plotted as a function of wind speed for several daily average insolation values. Also shown is the shape and amplitude of the diurnal cycle for different wind and insolation values. There are few low insolation values because TMI only measures between 40S and 40N. Rows A and B in Figure 1 show little variability from 1 AM to 8 AM. Warming can begin as early as 8 AM and is clearly seen in the 9 AM for data with high insolation values. From 9 AM onwards, all data with insolation greater than 132 Wm^{-2} show warming at low wind speeds. At the highest insolation and lowest wind speeds, warming reaches a peak value at 3 PM of 2.8°C. After 3 PM, the diurnal warming amplitude slowly subside, finally disappearing at midnight. Rows C and D show the wind and insolation dependence of the diurnal cycle. Warming increases with increasing insolation and decreasing wind speed. Both rows also show a cooling in the data from 6 AM through 8 AM at low wind speeds and high insolation. While not shown, ΔSST_{PF} exhibits a similar exponential dependence on wind speed and linear dependence on insolation. Two notable differences exist, ΔSST_{PF} has warming up to 10 ms^{-1}, while ΔSST_{TMI} only shows warming up to 6 ms^{-1}, and ΔSST_{PF} has warming down to zero insolation, while ΔSST_{TMI} only has warming above 132 Wm^{-2}. These differences could have several explanations: one of the algorithms might be in error (the TMI algorithm may have diminished response due removal of wind cross-talk, the PF regression algorithm is derived from

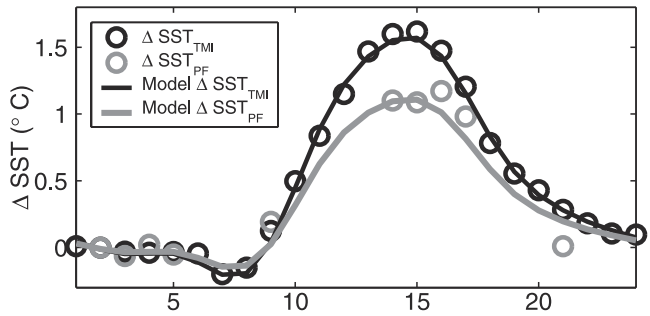

Figure 2. The diurnal cycle at 1.2 ms^{-1} wind speed and 320 Wm^{-2} insolation. Plotted on the figure are ΔSST_{TMI} (black circles), modeled ΔSST_{TMI} (black line), ΔSST_{PF} (gray circles), and modeled ΔSST_{PF} (gray line) as a function of local time.

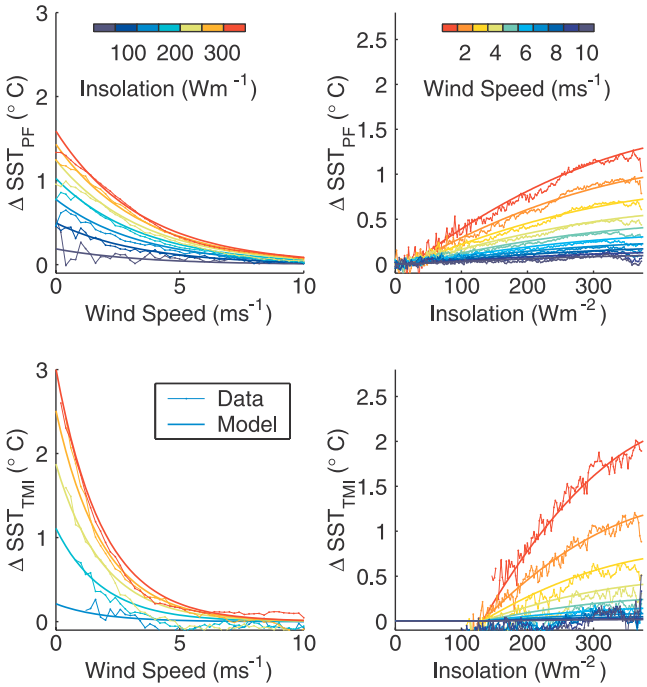

Figure 3. Comparison of data and empirical model at 2PM. The left column shows ΔSST_{PF} (top) and ΔSST_{TMI} (bottom) dependence on wind speed at several insolation values, indicated by line color. The right column shows the dependence on insolation at several different wind speeds.

collocations located primarily in a low-wind tropical regimes) or a physical reason that we do not yet understand.

[10] From these datasets, we calculated an empirical model of the diurnal warming using non-linear least-squares regression. Figure 1 shows a linear dependence on insolation, exponential dependence on wind speed, and a time dependence described by a five-term Fourier series. We derived ΔSST(°C), where Q is insolation (Wm^{-2}), t is time (hr) and u is wind speed (m/s), as follows:

$$\Delta SST_{tmi}(t,Q,u) = f(t)\left[\left(Q - Q_o^t\right) - 9.632\times10^{-4}\cdot\left(Q - Q_o^t\right)^2\right] \cdot e^{-0.53u}\} \text{ for } Q \geq Q_o^t \quad (1a)$$

$$\Delta SST_{pf}(t,Q,u) = 0.344 f(t)\cdot\left[\left(Q - Q_o^p\right) - 1.444\times10^{-3} \cdot\left(Q - Q_o^p\right)^2\right]\cdot e^{-0.29u}\} \text{ for } Q \leq Q_o^p \quad (1b)$$

$$f(t) = [6.814 - 6.837\cos(\omega t) - 8.427\sin(\omega t) + 1.447\cos(2\omega t) + 4.274\sin(2\omega t) - 0.407\cos(3\omega t) - 0.851\sin(3\omega t) + 0457\cos(4\omega t) - 0.555\sin(4\omega t) - 0.101\cos(5\omega t) + 0.375\sin(5\omega t)]\times 0.001$$

$$\omega = 0.2668 \text{ hr}^{-1}; Q_o^t = 132 \text{ Wm}^{-2}; Q_o^p = 24 \text{ Wm}^{-2};$$

[11] When solar heating is weak, below 132 Wm^{-2} (24 Wm^{-2}), there is no discernable diurnal cycle in the TMI (PF) data and the model is set to zero. Figure 2 shows a comparison of the TMI and PF SST data and modeled diurnal cycle at 1.2 ms^{-1} and 320 Wm^{-2} insolation. Since the shape of the diurnal cycle for the PF and TMI SST retrievals should be identical, a complete model can be

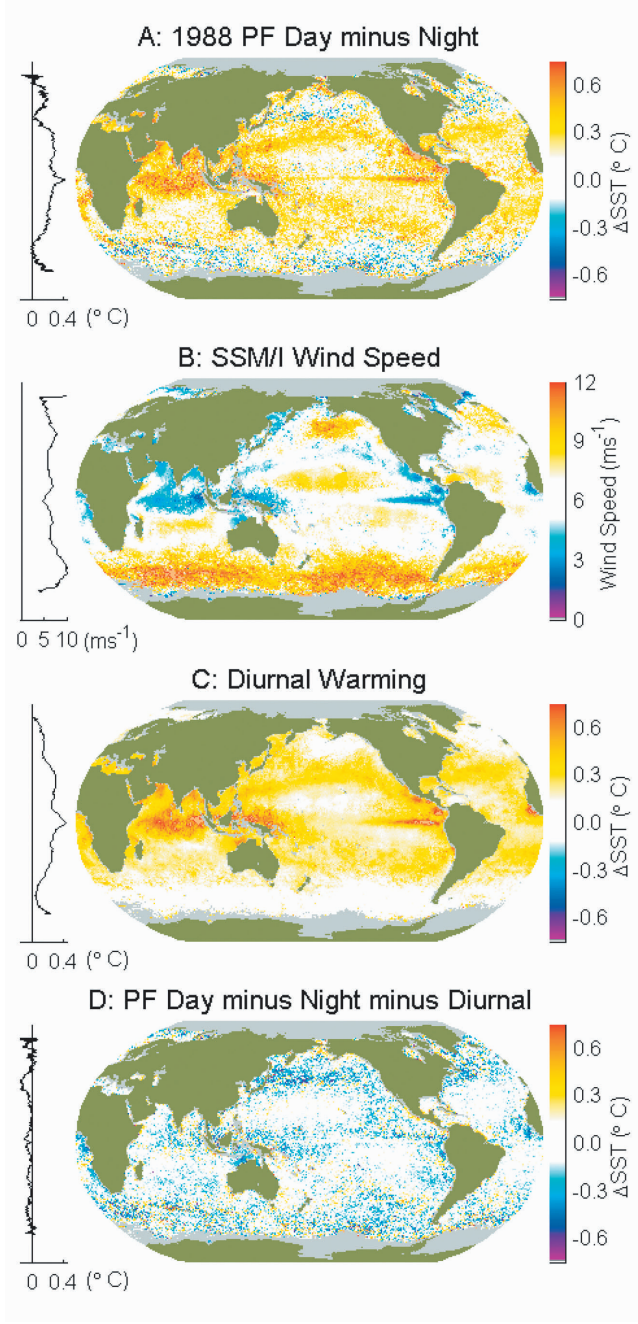

Figure 4. Diurnal warming during 1988. Figure 4a shows the annual average of PF day minus night SST, 4b: SSM/I wind speed, 4c: diurnal warm layer calculated with (1b), and 4d: PF day minus diurnal warming minus night SST. Gray indicates areas with missing PF SSTs, these regions were blocked out for all the other fields also. At the left side of each image, the mean value is shown as a function of latitude.

created for the PF, modeling the shape on the TMI diurnal cycle. In Figure 2, the PF data fits reasonably well to the modeled shape. The early morning minimum seen in Figure 1 is clearly revealed here. Although all diurnal warming has vanished by midnight, at low wind speeds there is a larger cool skin effect causing an early morning minimum. The amplitude of warming is larger in the TMI SSTs than in PF SSTs. We expect that the PF amplitude to be slightly underestimated, since without a time of observation for each PF SST retrieval we end up averaging over a range of local times due to swath width and orbital inclination. The model compares very well with the shape of the data; requiring only wind speed and daily average solar insolation as inputs. Figure 3 continues the comparison of our empirical model and data. It shows both data and model as a function of wind speed and insolation.

4. Discussion

[12] The distribution of diurnal warming is described in *Stuart-Menteth et al.* [submitted]. Large oceanic regions, at both mid-latitudes and the tropics, are affected by diurnal stratification, with the largest signal observed in the tropics and the northern Indian Ocean. There is a strong seasonal signal demonstrating how diurnal variability is dependent on the time of year. Regions experiencing frequent diurnal warming include the northern Indian Ocean during the intermonsoons, the Mediterranean Sea and mid-North Atlantic in boreal summer and the southern mid-latitudes in winter. Other regions in the tropics, the western Pacific and the waters off the west coast of Mexico are also highly susceptible to diurnal warming. These results highlight the need for the diurnal signal to be characterized in detail.

[13] Since SST variability during a single day is partly due to diurnal warming, a good test of our empirical model's ability to calculate diurnal warming is to compare the day minus night SSTs. On average, the mean difference and standard deviation should diminish when diurnal warming is removed from daytime retrievals. An example of this is shown in Figure 4 where daily diurnal warming was calculated and subtracted from daily average daytime PF SSTs. From top to bottom, Figure 4 shows day minus night PF SST, SSM/I wind speed, modeled diurnal warming, and day minus diurnal warming minus night PF SST averaged over 1988. Figure 4a shows that on average day PF SSTs are 0.22°C warmer (due to diurnal warming) and have a standard deviation of 0.8°C when compared to night PF SSTs. There are distinct regions of warming. The average SSM/I wind speeds (Figure 4b) show that the warm regions in Figure 4a correspond to regions of low wind speeds. Our modeled diurnal warming is shown in Figure 4c. Finally, Figure 4d shows the day minus diurnal minus night PF SSTs. The mean difference is reduced to −0.05°C and the standard deviation is diminished to 0.63°C. We repeated the procedure for the entire dataset, 1988 through 2001, in all cases the annual mean difference and standard deviations were reduced. Over the entire dataset, the day minus night PF SSTs difference is 0.22 °C and standard deviation is 0.68°C; while the daytime minus diurnal warming minus nighttime PF SSTs difference is −0.04°C and the standard deviation is 0.63 °C.

5. Conclusions

[14] TMI is the first satellite instrument to give accurate SST and wind speed data sampled throughout the diurnal cycle in the tropical regions. The magnitude of diurnal warming revealed by TMI can be large and persistent, typically lasting well into the night in regions of low wind speed. The presence of diurnal warming is independently verified by the PF SSTs at several points in the diurnal cycle, but exhibits a smaller peak than TMI at low wind speeds. TMI and PF measurements of diurnal warming as a function of wind speed and daily average insolation were used to derive an empirical model of diurnal warming. This model was applied to the daytime PF SST, successfully removing the majority of diurnal variability and decreasing the daytime minus nighttime variability. Development of a global diurnal model can help address the SST needs of both the climate and weather modeling by providing daily global SST fields 'normalized' to an 8 AM local time (the daily minimum in SST) alongside daily global diurnal amplitudes [*Wick*, 2002]. This will provide the climate community with an analysis free of diurnal variability and the modeling community with necessary diurnal information.

[15] **Acknowledgments.** This work was accomplished at Remote Sensing Systems supported by NASA contracts JPL-1228578 and TRMM NAS5-00217. The authors would like to thank Peter Minnett, Andy Harris, Ian Robinson, and two anonymous reviewers for helpful comments and guidance.

References

Donlon, C. J., P. Minnett, C. L. Gentemann, I. J. Barton, B. Ward, J. Murray, and T. J. Nightingale, "Towards operational validation of satellite sea surface skin temperature measurements for climate research", *J. Climate*, *15*(4), 353–369, 2002.

Kilpatrick, K. A., G. P. Podesta, and R. H. Evans, "Overview of the NOAA/NASA Pathfinder algorithm for Sea Surface Temperature and associated Matchup Database.", *J. Geophys Research*, *106*, 9179–9198, 2001.

Liou, Kuo-NaN, Solar radiation at the top of the atmosphere, in *An Introduction to Atmospheric Radiation*, *26*, 45–48, Academic Press, Inc., New York, 1980.

Price, J. F., R. A. Weller, and R. Pinkel, "Diurnal cycling: Observations and moels of the upper ocean response to diurnal heating cooling, and wind mixing", *J. Geophys. Res.*, *91*, 8411–8427, 1986.

Reynolds, R. W., and T. M. Smith, "Improved global sea surface temperature analyses using optimum interpolation", *J. Climate*, *7*, 929–948, 1994.

Stuart-Menteth, A. C., I. S. Robinson, and P. G. Challenor, "A global study of diurnal warming using satellite-derived sea surface temperature", submitted to *J. Geophys. Res.*

Wentz, F. J., C. L. Gentemann, D. K. Smith, and D. B. Chelton, "Satellite measurements of sea-surface temperature through clouds", *Science*, *288*(5467), 847–850, 2000.

Wentz, F. J., A well calibrated ocean algorithm for special sensor microwave/imager, *Journal of Geophysical Research*, *102*(C4), 8703–8718, 1997.

Wick, G. A., "The first report of the GHRSST-PP in situ and satellite data integration-technical advisory group", available from www.ghrsst-pp.org., 2002.

Yokoyama, R., S. Tanba, and T. Souma, "Sea surface effects on the sea surface temperature estimation by remote sensing", *Int. J. Remote Sens.*, *16*, 227–238, 1995.

C. L. Gentemann, Remote Sensing Systems, 438 First Street, Suite 200, Santa Rosa, CA 95401, USA. (gentemann@remss.com)

C. J. Donlon, CEC-Joint Research Centre, Space Applications Institute, Marine Environment Unit, Ispra, I-21030, TP272, Italy. (craig.donlon@jrc.it)

A. Stuart-Menteth, School of Ocean and Earth Science, Southampton Oceanography Center, Southampton, UK. (acsm@soc.soton.ac.uk)

F. J. Wentz, Remote Sensing Systems, 438 First Street, Suite 200, Santa Rosa, CA 95401, USA. (wentz@remss.com)